

LASER INTERFEROMETER GRAVITATIONAL WAVE OBSERVATORY
- LIGO -
CALIFORNIA INSTITUTE OF TECHNOLOGY
MASSACHUSETTS INSTITUTE OF TECHNOLOGY

Technical Note	LIGO-T1500123-v1	2015/10/08
Detector Characterization of the LIGO 40m Prototype Interferometer		
Eve Chase Mentors: Koji Arai and Maximiliano Isi		

California Institute of Technology
LIGO Project, MS 18-34
Pasadena, CA 91125
Phone (626) 395-2129
Fax (626) 304-9834
E-mail: info@ligo.caltech.edu

Massachusetts Institute of Technology
LIGO Project, Room NW22-295
Cambridge, MA 02139
Phone (617) 253-4824
Fax (617) 253-7014
E-mail: info@ligo.mit.edu

LIGO Hanford Observatory
Route 10, Mile Marker 2
Richland, WA 99352
Phone (509) 372-8106
Fax (509) 372-8137
E-mail: info@ligo.caltech.edu

LIGO Livingston Observatory
19100 LIGO Lane
Livingston, LA 70754
Phone (225) 686-3100
Fax (225) 686-7189
E-mail: info@ligo.caltech.edu

Abstract

The Advanced Laser Interferometer Gravitational-Wave Observatory (aLIGO) detectors will come online in the fall of 2015 with the goal of providing the first direct detection of gravitational waves. Detector characterization techniques, focused on the reduction of noise, are imperative to analyze and suppress noise to provide sufficient sensitivity for the detection of gravitational waves. Caltech houses the LIGO 40 meter prototype interferometer, a copy of the LIGO interferometers, providing the perfect playground to test and design novel detector characterization techniques for later implementation at the main sites. While summary pages, websites showing the state of the detector in real-time, are used to monitor the main detectors, the 40 meter prototype lacks many of these low-latency monitoring features. We incorporate new features into the 40 meter prototype summary pages in the hope of benefiting the entire LIGO community by providing real-time access to detector monitoring tools. Additionally, we develop basic tools to model Gaussianity of noise sources in a clear and visually meaningful display, open for addition to the summary pages.

Contents

1	Introduction	3
2	Summary Pages	4
2.1	Improvements to Existing Plots	6
2.2	Additions to the Summary Pages	7
2.3	System Improvements to the Summary Pages	9
3	Non-Gaussianity Tests of Noise Sources	9
3.1	Gaussianity Tests with Livingston Science Run 5 Data	11
4	Conclusion	16
5	Acknowledgments	16
	Appendix A Relevant Statistical Concepts	19
A.1	Arithmetic Mean	19
A.2	Variance	19
A.3	Standard Deviation	19
A.4	Skewness	19
A.5	Kurtosis	19
A.6	RMS	20
A.7	Fourier Transform	20
A.8	Fast Fourier Transform	20
A.9	Parseval's Theorem	20
	Appendix B How to Access the Summary Pages	22
	Appendix C Laguerre Expansion	23

1 Introduction

Einstein's General Theory of Relativity, a four-dimensional mathematical model of the dynamics of space-time, propelled a scientific hunt for the detection of gravitational waves with the formation of the dynamics of space-time. Einstein's theory predicts the existence of gravitational waves, ripples in space-time propagating at the speed of light, produced by the quadrupole moment of mass distribution [1]. Yet, nearly a century after their inception, gravitational waves have not been directly detected.

A worldwide network of ground-based interferometers has been constructed to provide the first direct detection of gravitational waves. The Laser Interferometer Gravitational-Wave Observatory (LIGO), consisting of detectors in Livingston, Louisiana and Hanford, Washington, recently underwent years of upgrades to provide greater sensitivity and increase the likelihood of detecting gravitational waves. To first order, these gravitational wave detectors are massive Michelson interferometers, with arm lengths of up to 4km (Figure 1) [3]. Laser light is split and sent down two orthogonal arms of equal length; the light is reflected at the end of the arms and then recombined. When a gravitational wave passes through an interferometer, a slight change in arm length will occur, resulting in a phase difference in laser light split down each arm. Gravitational wave signals are extracted from this resultant phase difference.

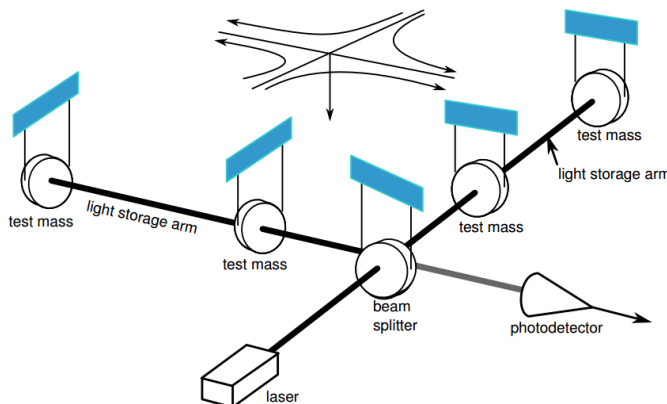


Figure 1: Basic interferometer design [2]

Detecting a gravitational wave is difficult and requires impeccably sensitive instrumentation and detection abilities, in an attempt to detect length variations of only 10^{-18} m, smaller than the diameter of a proton [3]. Noise makes detection even more difficult; everything in the interferometer system is moving or fluctuating, such as the mirror position, laser frequency, laser intensity, arm resonant condition, and many more factors resulting in a substantial number of noise sources. Gravitational wave detection is a battle against noise, and detector characterization spearheads this battle. Through detector characterization, we analyze interferometer output and noise sources for certain periods of time to characterize the nature of noise, in hopes of eliminating it from the data supply. Gravitational waves cannot be detected with LIGO without strong detector characterization techniques.

As Advanced LIGO becomes operational in late 2015 [4], the implementation of advanced

detector characterization techniques is imperative to utilize the increased sensitivity for direct detection of gravitational waves. I am pleased to have devoted my summer to LIGO detector characterization while it serves a vital role in the effort to detect gravitational waves.

My summer project consists of two main parts, outlined in this paper. As described in Section 2, I updated the LIGO summary pages which facilitate detector monitoring tasks. Subsequently, I characterized non-Gaussian noise through various statistical methods as described in Section 3. Relevant statistical concepts are listed in Appendix A, and instructions for accessing and editing the summary pages are found in Appendix B.

2 Summary Pages

In addition to the two large LIGO detectors in Washington and Louisiana, Caltech houses a prototype detector [5]. The prototype detector, with 40m long interferometer arms, has a similar configuration to the larger detectors but is more open to modification and testing of new design implementations (Figure 2). The 40m prototype detector is the perfect playground for detector characterization experimentation. By implementing new designs at the 40m detector instead of the LIGO sites, we are able to provide novel improvements to all LIGO detectors without interfering with data collection at the sites. The prototype consists of several subsystems which monitor the functionality of the detector, enumerated in Table 1 [6, 7, 8]. By frequently collecting data from the subsystems, we provide a means of monitoring the detector.

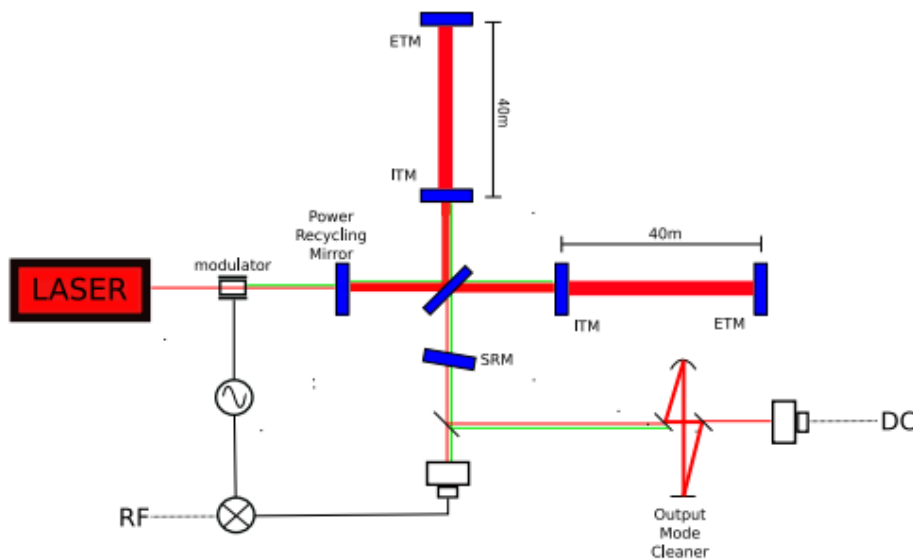


Figure 2: Schematic representation of the 40m prototype detector. A length of 40m separates the input mirror (ITM) and end mirror (ETM) [5, 6].

LIGO summary pages provide an accessible method to monitor the detectors in real time online [9]. Summary pages include dozens of plots monitoring detector status from seismic activity, to suspension systems, and to lock status. Summary pages include ASD spectra

Table 1: 40m Detector Subsystems

Name	Subsystem Details
Length Sensing and Control (LSC)	Mirror position control and gravitational wave signal channel.
Angular Sensing and Control (ASC)	Mirror angular control.
Arm Length Stabilization (ALS)	Monitor x and y arm length.
Pre-Stabilized Laser (PSL)	Optical cavities for laser stabilization in frequency and spacial distribution.
Input and Output Optics (IOO)	Similar to PSL.
Suspensions (SUS)	Sensors for mirror positions and angles. Optical lever system which provides additional angular sensing signals.
Physical Environmental Sensors (PEM)	Seismic and acoustic noise.
Vacuum System (VAC)	Vacuum status monitoring.

displaying gravitational wave amplitude spectral density over frequency [10]. Summary pages also provide time-frequency event plots representing signal-to-noise ratio (SNR) for several event triggers [10]. A screenshot of summary pages is shown in Figure 3. While the Hanford and Livingston detectors have highly informative summary pages, the 40m summary pages are far behind the quality of the Livingston and Hanford summary pages and lack much of the information represented in the latter two [9, 11, 12]. This summer, we have implemented several new features and plots into the 40m summary pages, to enhance the readability and usability of the summary pages for all members of the LIGO community.

Production of summary pages for the 40m prototype requires careful configuration of many channels from many subsystems of the prototype. We analyze each channel for a set period of time to determine the nature of each signal. While checking the behavior of signals, we may reveal problems with the functionality of specific subsystems of the detector, contributing to detector improvement.

Summary pages are produced using the `GWsumm` [13] toolbox, which is based on the `GWpy` [14] Python package, providing tools to load, assess, and plot LIGO data. `GWsumm` [13] scripts can provide plots for data channels and associated HTML to post the plots on the summary page website. Instructions for editing and producing the 40m summary pages can be found in Appendix B.

We sought to provide useful and informative additions to the summary pages to help all

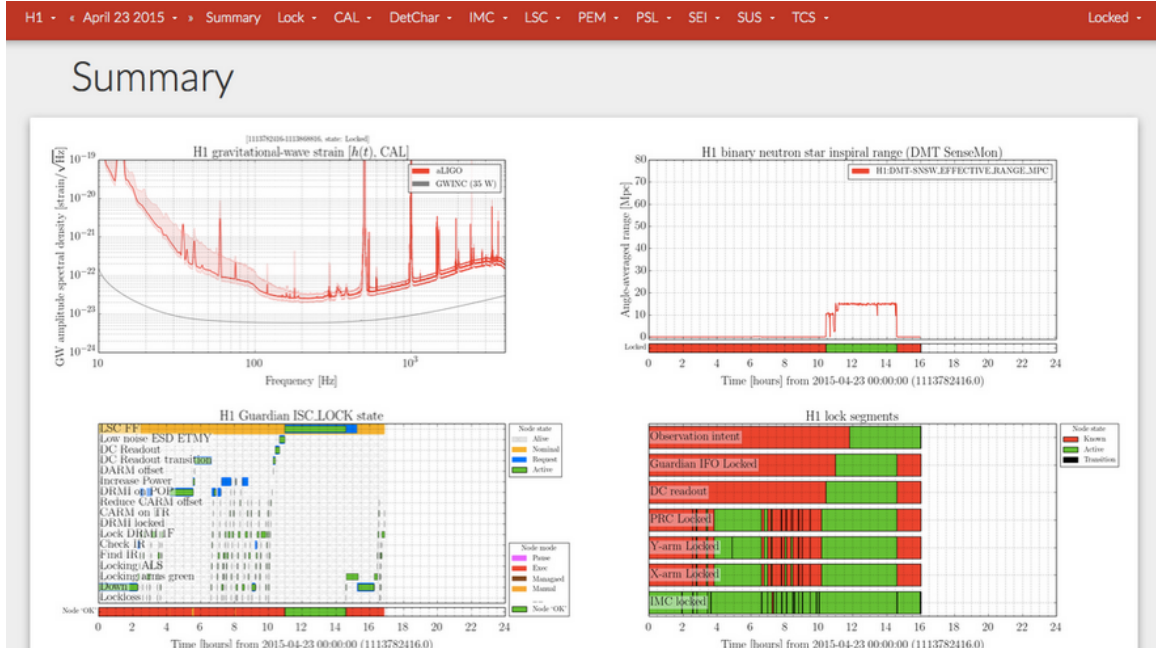


Figure 3: Screenshot of a summary page monitoring the Hanford detector [12].

users of the 40m detector. After speaking with commissioners of the 40m detector, we implemented improvements to the summary pages that they viewed as necessary. We enumerate improvements and additions to the summary pages in the following sections.

2.1 Improvements to Existing Plots

Several plots were already available on the summary pages, before the start of this summer project, including those for IOO, PEM, PSL, SUS, and VAC subsystems, but many of these plots required improvements. We first provided improved titles and axis labels, as many plots lacked appropriate labeling.

In addition to providing cosmetic adjustments to either the dearth or flaws in labels, we altered the range of axes in many cases. Occasionally, axis ranges that failed to appropriately display the necessary data were selected. We determined appropriate axis ranges by observing past data from several months at a time on the *DataViewer* [15] program present at the 40m detector, and we implemented appropriate axis ranges into the summary pages.

There are several periods of time during which no data is displayed on the summary pages, causing confusion as to what is causing the break in data and uncertainty if data is not being collected or if the data collected is not within the axis ranges of the summary page plots. By monitoring the channels in question on *DataViewer* [15], we analyzed the cause of such breaks in data acquisition and implement changes to the summary pages, appropriately.

The summary pages lacked accurate triggering systems for certain plot rendering processes. Specifically, we want to only render data when the interferometer is locked. For example, the channels `C1:IOO-MC_TRANS_P` and `C1:IOO-MC_TRANS_Y` should only be plotted when the mode cleaner is locked, namely when `C1:IOO-MC_TRANS_SUM` is greater than 10^4 counts. We

altered the summary pages configuration files to allow the user to choose between rendering data for all times or only for times at which the mode cleaner is locked, such as in Figure 4. The addition of triggered states allows for more practical and legible data visualization.

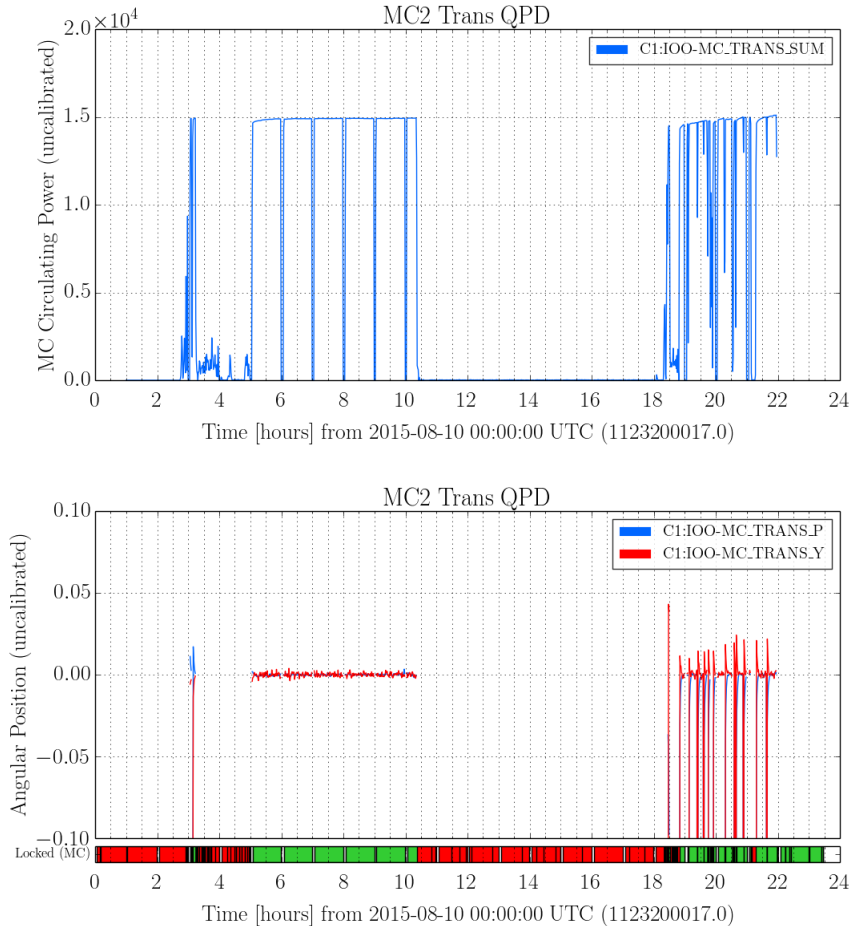


Figure 4: A “state” function is added to the 40m summary pages to restrict data rendering to times at which the mode cleaner (MC) is locked. This is implemented into the IOO summary page tab, at which the user can select either All or Locked (MC) from a drop-down menu to visualize data accordingly. The top plot represents uncalibrated power over time, and the plot on the bottom represents uncalibrated difference in position of a sensor.

At the request of a 40m commissioner, weather plots were improved to include more temperature information. While PSL table temperature and outdoor temperature, recorded at the 40m detector weather station, were already present in the summary pages, we added indoor temperature, as recorded by the C1:PEM-weather_insideTemp channel, to the existing temperature plot on the Weather tab.

2.2 Additions to the Summary Pages

We added plots to these sections of the summary pages. Six suspension system optical level (OpLev) plots already exist on the summary pages and represent optical lever fluctuations

in microradians over time for numerous channels. We produced spectra for each OpLev plot and displayed the spectra tangentially to the already existing time-series, to provide an easy means of visually comparing the data. Two such plots are shown in Figure 5.

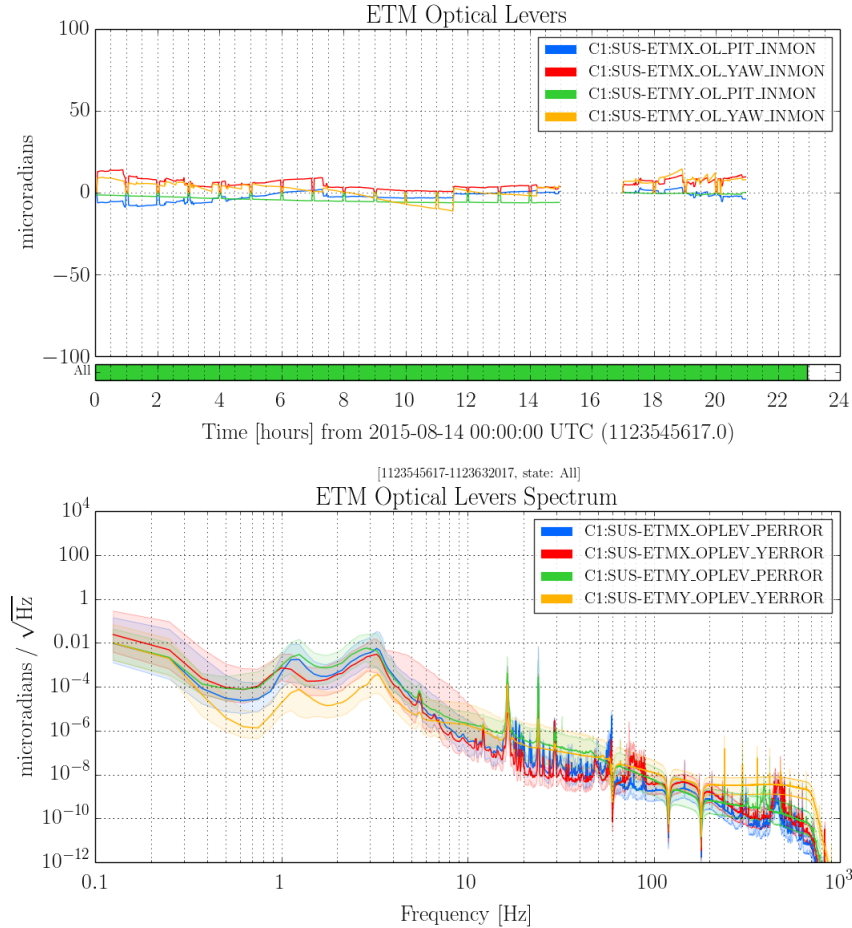


Figure 5: In the SUS: Oplev tab of the 40m summary pages, a time-series of four optical lever channels is displayed tangentially to an ASD of the corresponding error channels to each of these four channels.

The summary pages include many plots representing suspension systems for the 40m interferometer. The SUSdrift tab previously included information on the position of the input mode cleaner (IMC) and suspension test masses, through angular measurements. We added two plots to the SUSdrift tab to record angular position of the dual-recycling Michelson interferometer (DRMI), for both pitch and yaw.

Three tabs were added to the summary pages to provide monitoring information not previously displayed on the website. The Arm Length Stabilization (ALS) tab was created, with two time-series characterizing green laser transmission and beatnote. The new Angular Sensing and Control (ASC) tab monitors position in the input mode cleaner and both interferometer arms. Lastly, the Length Sensing and Control (LSC) tab was created to display a cavity power time-series for multiple channels.

2.3 System Improvements to the Summary Pages

The summary pages online interface includes a code status page, which records the time at which the summary pages were last updated and various error messages associated with the different tabs of the summary pages. Previously, the code status page would record each tab as either `OK` or `ERROR`. The code status page failed to recognize instances in which tab rendering resulted in a warning message and, instead, categorized this as an error. The code status page was improved to list `WARNING` as a third tab status, thus providing a more obvious interface.

3 Non-Gaussianity Tests of Noise Sources

While not working on implementation of summary pages, we focused on noise characterization. We explored the appearance of various noise sources in the interferometer channels and provide additional methods to characterize noise with the predefined goal of eliminating as many noise sources as possible from the detector.

Gravitational wave detectors are constantly inundated with noise. Noise comes in numerous forms, such as white noise, sinusoidal, stochastic, Gaussian, and more. Noise can be classified as deterministic, such as sinusoidal or periodic noise, or indeterministic noise, such as stochastic noise (random and continuous) or random bursts. We can assign a color to noise, which is associated with the slope of the noise’s power spectrum. White noise is flat while pink noise is enhanced at lower frequencies. We categorize noise as Gaussian or non-Gaussian, dependent on the statistical nature of the noise. Typically, thermal and quantum noise exhibit Gaussian behavior. It is difficult to distinguish between transient gravitational wave events and non-Gaussian noise, specifically in gravitational wave searches without predefined waveforms (i.e. burst searches), thus requiring the characterization of non-Gaussian noise to reveal true event signals [16]. By characterizing noise Gaussianity, we can better recognize noise patterns and understand the nature of noise, leading to the further elimination of many noise sources.

Power spectral density (PSD) provides one means to characterize noise distributions. A PSD is a measure of power in several frequency bands, averaged over time. The Fourier transform of $\tilde{x}(f)$ of a time-series $x(t)$ is, by definition:

$$\tilde{x}(f) = \int_{-\infty}^{\infty} x(t)e^{-i2\pi ft} dt, \quad (1)$$

where $|\tilde{x}(f)|^2$ provides the energy spectral density. Energy spectral density abides by Parseval’s theorem, which ensures that signal power computed in both the frequency and time domains are the same, described in Appendix A.9. When noise or signal extends infinitely in the time-domain, we can define the PSD [17, 18, 19]:

$$\lim_{T \rightarrow \infty} \frac{1}{T} |\tilde{x}(f)|^2. \quad (2)$$

PSDs also follow Parseval’s theorem and correct calculation of a PSD can be confirmed using this theorem. A PSD has units equivalent to the units of $|x(t)|^2$ divided by Hz. Typically,

in gravitational wave data analysis, we represent our PSDs in strain / $\sqrt{\text{Hz}}$. This requires us to take the square root of our PSD, which forms an amplitude spectral density (ASD). Colloquially, ASDs are often still called PSDs, despite this change in calculation.

We calculate PSDs of interferometer signals for a given short period of time, providing many useful applications in detector characterization. For example, PSD calculation allows us to monitor the violin, roll, and bounce modes of the steel wires used to suspend the interferometer's mirrors [20, 21]. Each mirror has six rigid body degrees of freedom: longitudinal, side, vertical, pitch, yaw, and roll. The resonances of each of these six modes has low dissipation, corresponding to a long ringdown mode, or high quality factor (Q) for the modes. Feedback damping is used to lower the Q 's for some modes, but the violin, roll, and vertical (or bounce) modes have no such damping control and occasionally become excited by seismic motion or cross-coupling between modes. Characterization of noise from these three modes can be achieved through the calculation of a PSD.

By following the statistical method, enumerated in [16], we statistically characterize Gaussianity of PSDs. Assuming we sample the detector output, $v(t)$, in time intervals of Δt , the raw output data is recorded as $v_j = v(j\Delta t)$. From the output data, we calculate the output power:

$$P_j = |v_j|^2. \quad (3)$$

By dividing the output data into n segments, with k data points in each segment, we define the following quantities derived from power:

$$P_0 \cong \overline{P_j} \quad (4)$$

$$P_1 = \frac{1}{k} \sum_{j=1}^k P_j \quad (5)$$

$$P_2 = \frac{1}{k} \sum_{j=1}^k (P_j)^2, \quad (6)$$

where P_0 is the long-term average of P_j , using all data points. P_1 is the instantaneous mean of signal power, P_j , given for only a single data segment. Similarly, P_2 is the instantaneous mean of the squared signal power, also for only a specific segment. The parameter $\overline{P_j}$, is the average of P_j . If data are completely stationary, P_j is constant, resulting in a P_1 equal to P_0 , and P_2 equal to P_0^2 for all n data segments. From these parameters, we define two Gaussianity evaluations coefficients:

$$c_1 = \frac{P_1}{P_0} - 1 \quad (7)$$

and

$$c_2 = \frac{1}{2} \left(\frac{P_2}{P_1^2} - 2 \right), \quad (8)$$

which are also the first two coefficients in the Laguerre expansion of the noise power distribution, found by equating $P(\zeta)$ in Appendix C and $P(j)$. It is assumed that c_2 becomes constant if the signal power is much larger than the background noise level [16]. The coefficient c_1 provides a metric for the stability of a signal, while c_2 indicates non-Gaussianity, as P_2/P_1^2 is related to glitchiness of power.

Using the coefficients c_1 and c_2 , we can evaluate the Gaussianity of a PSD. If $P(j)$ obeys a normal Gaussian distribution, $c_1 = c_2 = 0$. Fluctuations in the average power, P_1 , result in a non-zero c_1 . If P_j follows a Gaussian distribution with a non-unity standard deviation, c_1 becomes non-zero, but c_2 remains zero, as an indication of the signal's Gaussian nature.

Rayleigh statistics provide another means to determine the Gaussianity of a noise distribution [7, 22], historically more common in the LIGO community. The Rayleigh statistic (R) provides a metric for the Gaussianity of noise through a calculation of the ratio of standard deviation to mean of a power spectrum in a set frequency bin:

$$R(f) = \frac{\sigma[|\tilde{x}_T(f)|^2]}{\mu[|\tilde{x}_T(f)|^2]}, \quad (9)$$

where σ and μ are defined in Appendix A and $\tilde{x}_T(f)$ is defined in Equation 1. The value of R provides a numerical measure of the Gaussianity of a signal, with $R = 1$ representing Gaussian noise, $R < 1$ representing coherent variation in the data, and $R > 1$ indicating that glitchy data is present [7, 22, 23]. Rayleigh statistics are based on the assumption that an exponential distribution, with an equal mean and standard deviation, suggests a Gaussian noise signal.

We can equate the statistical applications of Rayleigh statistics with the coefficient analysis of PSDs in [16]. For a given PSD, we expect P_1 to be the mean:

$$P_1 = \mu \left[\frac{1}{T} |\tilde{x}_T(f)|^2 \right], \quad (10)$$

and P_2 to follow the distribution,

$$P_2 = \left(\sigma \left[\frac{1}{T} |\tilde{x}_T(f)|^2 \right] \right)^2 + P_1^2. \quad (11)$$

From this, we derive the equation for R in terms of P_1 and P_2 :

$$R^2 = \frac{P_2 - P_1^2}{P_1^2} = \frac{P_2}{P_1^2} - 1. \quad (12)$$

It is then evident that

$$c_2 = \frac{1}{2}(R^2 - 1), \quad (13)$$

to match Equation 8. For a Gaussian distribution, R is one and c_2 is zero.

We implemented our statistical metrics for Gaussianity of PSDs to a sample set of data from LIGO's Science Run 5 (S5). We provide a visually explicit model for characterizing the Gaussianity of noise, through the c_2 coefficient, for the complete frequency range of the corresponding PSD, as described in the following section.

3.1 Gaussianity Tests with Livingston Science Run 5 Data

We downloaded an hour of Livingston S5 data from the LIGO Open Science Center (LOSC) [24] as an hdf5 file. Using the `readligo` module, also available at LOSC, the data are

stored into a series of Python data structures, which include information on strain, time, and channel information.

By plotting strain versus time, we produced a time-series for 16 seconds of data from the hour of downloaded data (Figure 6). The data are chaotic and conveys little information in the time-domain. Some oscillatory periods can be determined from these plots, but much more information is available if we observe the same dataset in the frequency-domain.

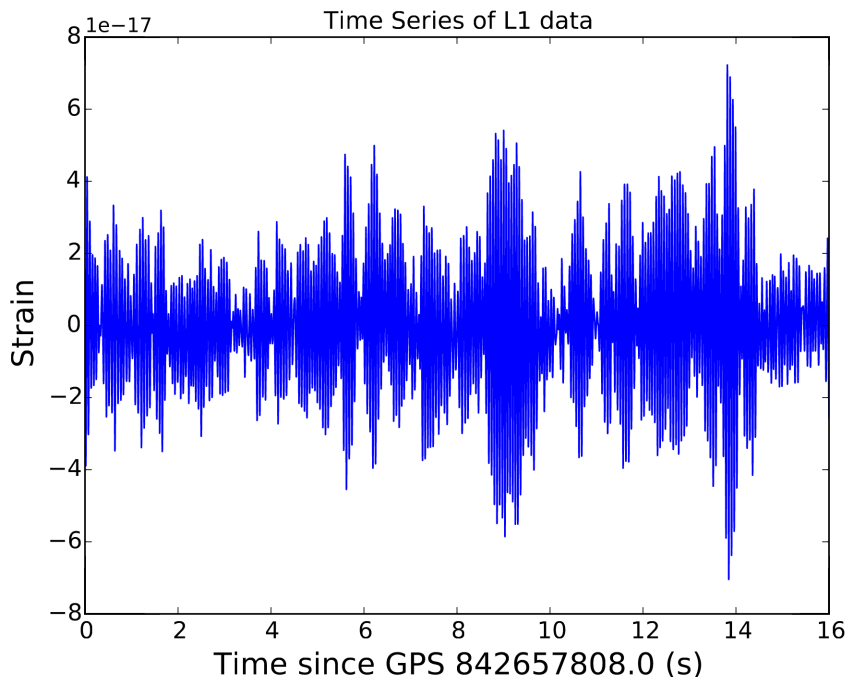


Figure 6: Strain versus time for 16 seconds of L1 data from S5.

We create a PSD of the dataset to provide more information about the frequency content of the time-series. We use the Python function, `matplotlib.mlab.psd()` to compute the PSD. This function uses Welch’s average periodogram method to approximate a PSD. The time-series is divided into several segments of length $NFFT$, and the fast Fourier transform (see Appendix A) is calculated for each segment, then squared, and then averaged for all segments to produce the PSD. We define the sampling frequency to be the inverse of the time between consecutive data sampling. The $NFFT$ segment length is also set to this sampling frequency value. We select a Hanning window function, which maps each segment’s values onto the Hanning function of length $NFFT$. As the Hanning function eliminates datapoints at the endpoints of segments, we define an overlap of half of $NFFT$ which recalculates the PSD using the same segments shifted over by half their lengths. Using this method, we produce the PSD seen in Figure 7. This PSD looks very similar to that of the Livingston detector during the S5 run, with several frequency peaks appearing in the expected locations (Figure 8). To directly compare Figure 7 and Figure 8, the y-axis of Figure 8 must be divided by the length of the interferometer arms, 4km. We confirm the calculation of our PSD by ensuring that Parseval’s theorem holds, by following Equation 27 in Appendix A.

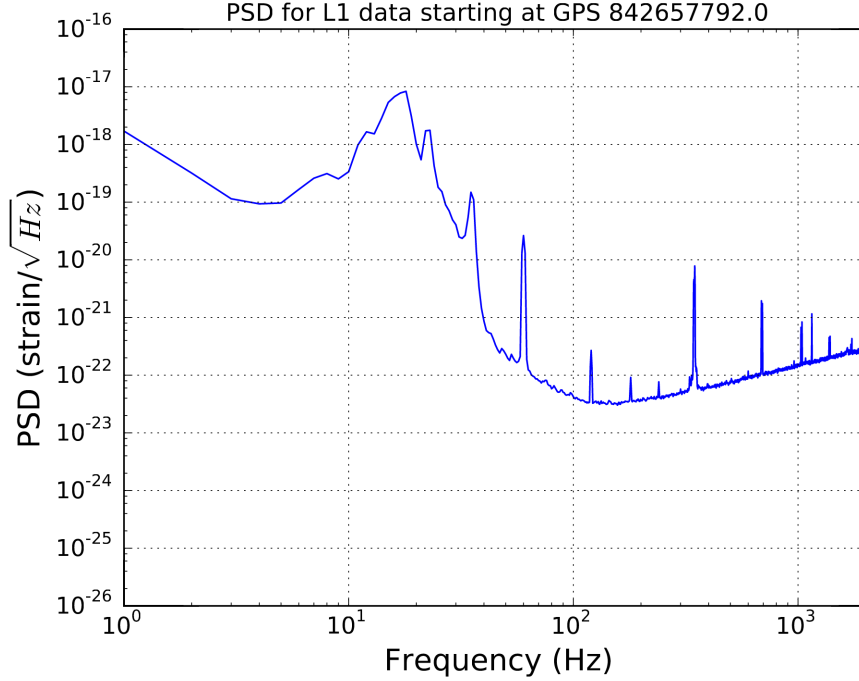


Figure 7: PSD calculated over entire time-series dataset for a set of Livingston S5 data.

We begin to explore the Gaussianity of LIGO data at individual frequency values by compiling distribution statistics for a series of PSDs. We split the time-series of Figure 6 into several equally spaced frequency chunks of 1 second length, overlapped with half of the chunk length, and calculate the individual PSD of each chunk. We plot the PSD produced for each segment on the same plot and compare them (Figure 9). At a specific frequency, we view the spread in PSD value through the production of a histogram. A histogram for the spread in PSDs at 1000Hz is shown in Figure 10. We display the distribution in the pure PSD, with units of $1/\sqrt{\text{Hz}}$, to clearly show that an exponential distribution represents Gaussian noise.

We then follow the mathematical metric of [16] to calculate the c_2 coefficient for Gaussianity at each frequency. The long-term average, P_0 (Equation 4), is calculated by taking the maximum number of time chunks that the time-series can be divided into and averaging all PSD values at a given frequency. The instantaneous average, P_1 (Equation 5), is calculated with the same method for a smaller number of time chunks. Using these coefficients, in addition to P_2 (Equation 6), we follow Equation 8 to calculate the c_2 coefficient. Figure 11 shows the c_1 and c_2 coefficients at each frequency for a given PSD.

From this mathematical metric, we can highlight particularly illuminating frequencies, with highly non-Gaussian behavior. For example, peaks at 23Hz and 33Hz appear to have no major difference in statistical characteristics in Figure 9, but differ greatly when c_2 is calculated. The 23Hz band (Figure 12) has a c_2 of -0.474, suggesting a stationary noise distribution, while the 33Hz band (Figure 13) exhibits a highly glitchy distribution with a c_2 of 0.888.

By directly calculating c_2 for a set of PSDs at a given frequency, we are able to characterize the Gaussianity of noise far beyond the level that is available by visually observing the PSD.

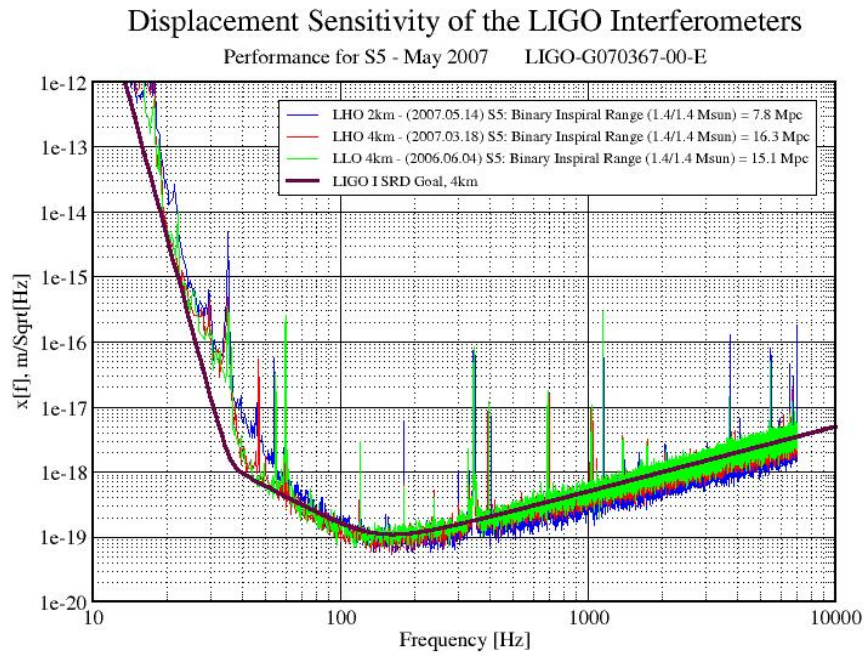


Figure 8: Published sensitivity for the LIGO detectors during the S5 run [25].

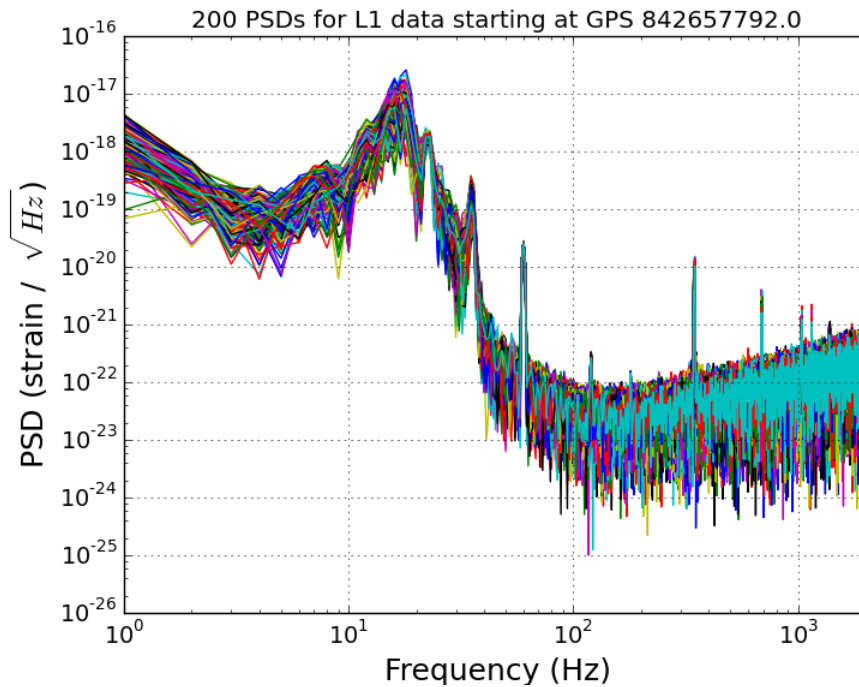


Figure 9: Several PSDs calculated for equally spaced frequency segments and compiled into one graph.

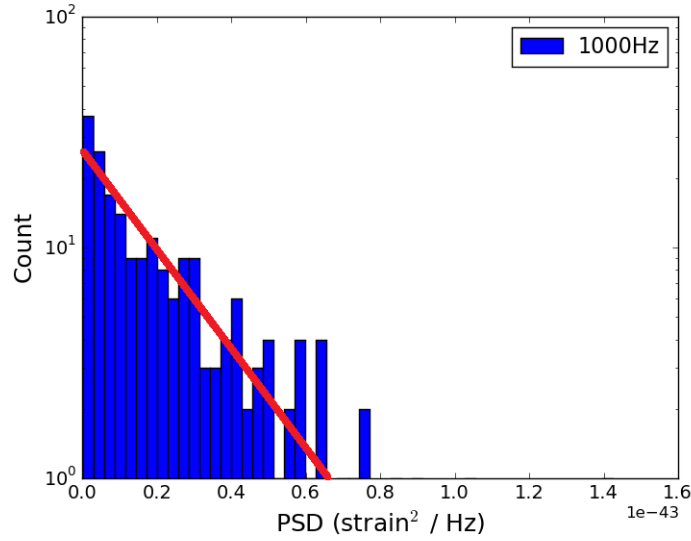


Figure 10: A clear exponential distribution is present in the PSD spread at 1kHz, suggesting Gaussian noise. The red line displays an exponential distribution, which appears linear in a log-lin plot.

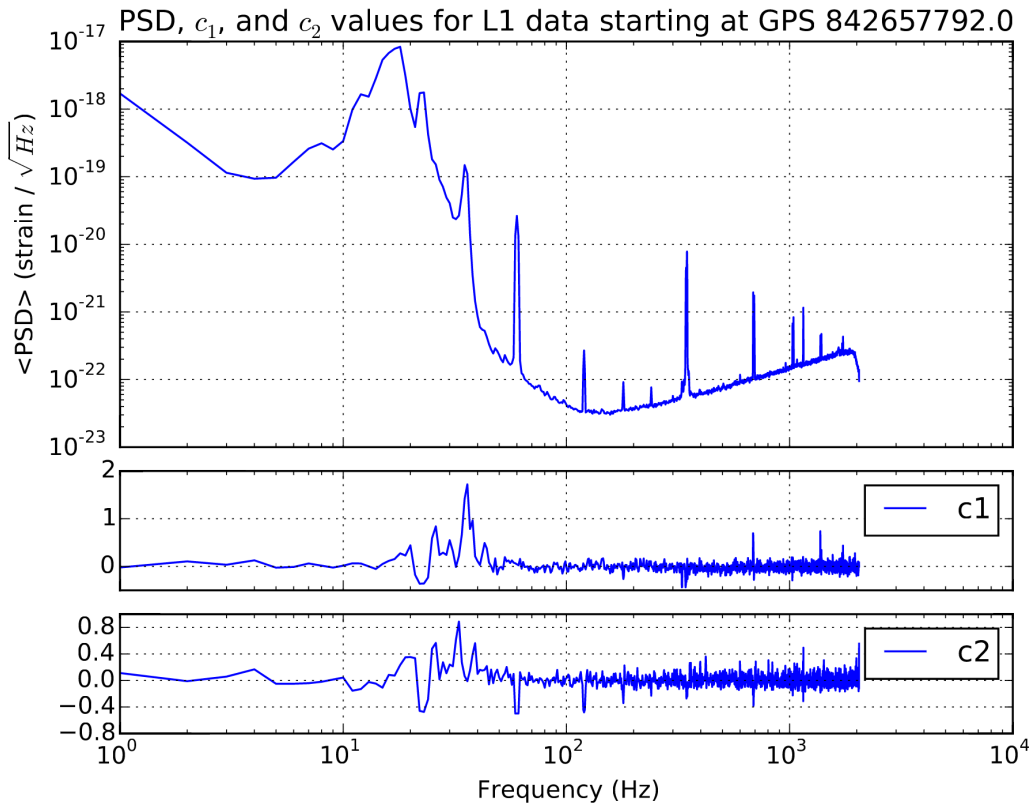


Figure 11: Average of the many PSDs, displayed in Figure 9, with corresponding c_1 and c_2 coefficients. A c_2 of zero indicated Gaussian noise at a particular frequency.

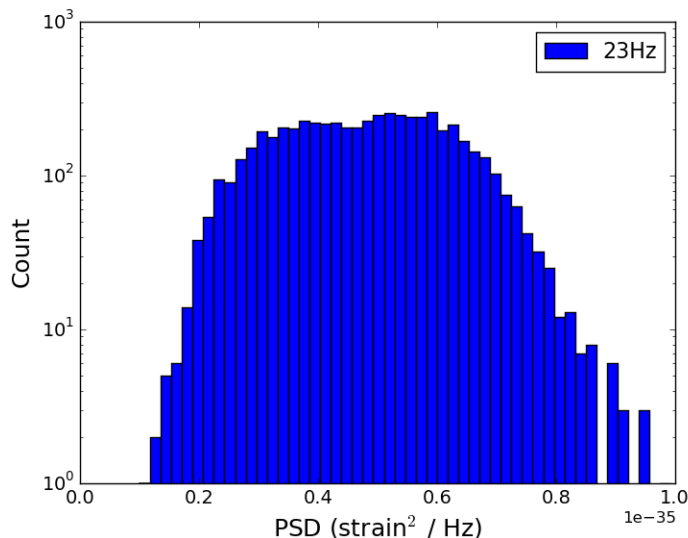


Figure 12: A stationary noise distribution is present at 23Hz.

Gaussianity plots, such as Figure 11, provide a clear method of visualizing noise distributions at a wide range of frequencies. This method can be expanded upon by providing plots to observe the change in Gaussianity for a signal at a particular frequency over time.

4 Conclusion

As Advanced LIGO begins to collect data, detector characterization takes a vital role in the effort to locate gravitational wave signals in these data. The implementation of summary pages for the 40m prototype detector benefits the entire LIGO community by providing real-time access to detector monitoring tools. Characterization of noise Gaussianity through a mathematically rigorous model leads to a clear method of understanding and observing noise in many channels of the interferometer, enhancing later data collection and eventual astrophysical data analysis of the interferometer output. In the future, Gaussianity plots, such as Figure 11 can be added to the 40m summary pages, in addition to the main detector summary pages, to provide further information on the detector channels.

5 Acknowledgments

This work is supported through the Caltech LIGO SURF program, in addition to the LIGO REU program supported by National Science Foundation award 1460838. I would especially like to thank my mentor, Koji Arai, for the vast amount of care, attention, and enthusiasm for my SURF project throughout the summer. I also greatly appreciate the assistance and support from Max Isi. Thank you to my fellow 40m SURF students, Ignacio Magana, Jessica Pena, and Megan Kelley for a fun summer, and to 40m regulars EricQ, Jamie, and Steve for additional help throughout the summer.

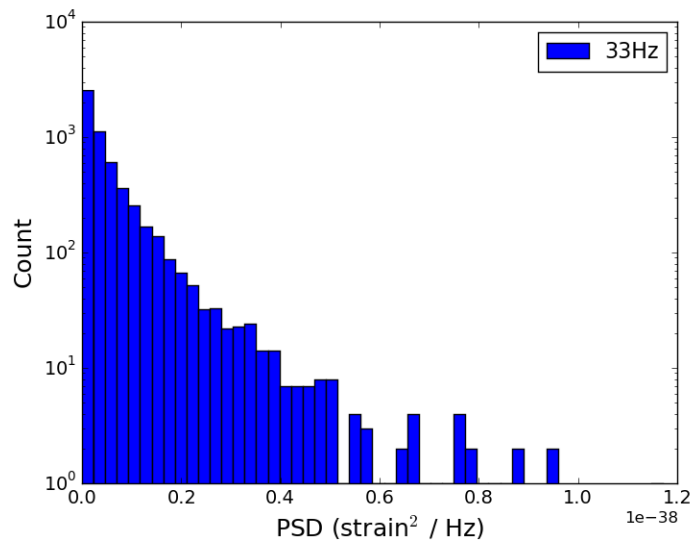


Figure 13: A glitchy noise distribution is present at 33Hz. Instead of having a distinct exponential decay, some excess PSD signal is present at higher PSD values, indicating non-Gaussian noise.

References

- [1] Flanagan, E. & S. Hughes. *The basics of gravitational wave theory*. New J.Phys. 7, 204 (2005).
- [2] http://www.ligo.caltech.edu/LIGO_web/PR/scripts/draw_lg.html
- [3] Abbott, BP et al. *LIGO: the Laser Interferometer Gravitational-Wave Observatory*. Rep. Prog. Phys. 72, 076901 (2009).
- [4] <https://www.advancedligo.mit.edu/>
- [5] Ward, RL et al. *DC Readout Experiment at the Caltech 40m Prototype Interferometer*. Class. Quantum Grav. 25, 114030 (2008).
- [6] Izumi, K. et al. *Multicolor cavity metrology*. J. Opt. Soc. Am. 29, 10, 2092 (2012).
- [7] Davison, E. *Detector Characterization Tools for Interferometer Commissioners*. LIGO-G1200818-v1 (2012).
- [8] Abbott, B. et al. *LIGO Caltech 40-Meter Prototype Procedures Manual*. LIGO-T03xxxx-00-D (2003).
- [9] *LIGO C1 Summary Pages*. <http://www.ligo.caltech.edu/~misi/summary/>
- [10] Macleod, D. *How to read the (LIGO) summary pages*. LIGO-G1401357-v2 (2014).
- [11] *LIGO L1 Summary Pages*. <https://ldas-jobs.ligo-la.caltech.edu/~detchar/summary/>

- [12] *LIGO H1 Summary Pages*. <https://ldas-jobs.ligo-wa.caltech.edu/~detchar/summary/>
- [13] Macleod, D. *Gravitational-wave interferometer summary information system*. <https://github.com/gwpy/gwsumm>
- [14] Macleod, D. *GWpy*. <https://gwpy.github.io/>
- [15] Macleod, D. *Gravitational-Wave Data Viewer*. <https://github.com/gwpy/dataviewer>
- [16] Ando, M. et al. *Methods to characterize non-Gaussian noise in TAMA*. *Class. Quantum Grav.* 20, S697 (2003).
- [17] Kanner, J. *Introduction to LIGO data analysis*. LIGO-G1500862 (2015).
- [18] Shawhan, P. *Gravitational-Wave Data Analysis: Lecture 1*. LIGO-G1300036-v1 (2012).
- [19] Blandford, R. & K. Thorne. *Random Processes*. In *Applications of Classical Physics*. (2012).
- [20] Lockerbie, N. & K. Tokmakov. *Violin-Mode Detection– Conclusion*. LIGO-G1000954-v1 (2010).
- [21] Shapiro, B. *Tuned Mass Damper Simulations for Quad Bounce and Roll Modes*. LIGO-T1500271-v7 (2003).
- [22] Sutton, P. & P. Saulson. *RayleighMonitor Overview*. LIGO-G040422-00-Z.
- [23] Finn, L., Gonzalez, G. & P. Sutton. *RayleighMonitor: A Time-Frequency Gaussianity Monitor for the DMT*. LIGO-G020133-00-Z (2002).
- [24] *LIGO Open Science Center*. <https://losc.ligo.org/>
- [25] *Displacement Sensitivity of the LIGO Interferometers*. http://www.ligo.caltech.edu/~l1_news/s5_news/s5002.jpg
- [26] *Fast Fourier Transforms*. <http://hyperphysics.phy-astr.gsu.edu/hbase/math/fft.html>

Appendix A Relevant Statistical Concepts

A.1 Arithmetic Mean

The arithmetic mean represents an unweighted average of a set of n values.

$$\mu = \bar{x} = \frac{1}{n} \sum_{i=1}^n x_i \quad (14)$$

A.2 Variance

Variance, σ^2 , measures the spread of a set of numbers.

$$\sigma^2 = \frac{1}{n} \sum_{i=1}^n (x_i - \mu)^2 \quad (15)$$

A.3 Standard Deviation

Standard deviation is the square root of variance. It represents the amount of variation in a set of n values.

$$\sigma = \sqrt{\frac{1}{n} \sum_{i=1}^n (x_i - \mu)^2} \quad (16)$$

A.4 Skewness

Skewness quantifies the asymmetry of a distribution. If the left side is more pronounced than the right side, then the data set is said to have negative skewness. If the distribution is symmetric, skewness is zero. Equations for skewness vary, and one such equation is provided below.

$$Skewness = \frac{\frac{1}{n} \sum_{i=1}^n (x_i - \mu)^3}{\sigma^3} \quad (17)$$

A.5 Kurtosis

In addition to skewness, kurtosis provides another descriptor for the shape of a distribution. Kurtosis is represented in many ways, of which one such equation is provided, and can be thought of as “peakedness” of a distribution.

$$Kurtosis = \frac{\frac{1}{n} \sum_{i=1}^n (x_i - \mu)^4}{\sigma^4} \quad (18)$$

A.6 RMS

The root mean square (RMS) can be calculated to represent a series of data points varying with time. The RMS for a set of n discrete values is:

$$x_{rms} = \sqrt{\frac{1}{n}(x_1^2 + x_2^2 + \cdots + x_n^2)}, \quad (19)$$

while the RMS for a continuous time-dependent function from the time interval T_1 to T_2 is

$$f_{rms} = \sqrt{\frac{1}{T_2 - T_1} \int_{T_1}^{T_2} [f(t)]^2 dt}. \quad (20)$$

A.7 Fourier Transform

The Fourier transform provides a continuous Fourier series from $-\infty$ to ∞ for a given function. The Fourier transform of $f(t)$ is,

$$g(\omega) = \frac{1}{2\pi} \int_{-\infty}^{\infty} f(t)e^{-i\omega t} dt, \quad (21)$$

and the inverse Fourier transform is,

$$f(t) = \int_{-\infty}^{\infty} g(\omega)e^{i\omega t} d\omega. \quad (22)$$

A.8 Fast Fourier Transform

The fast Fourier transform (FFT) provides a computer algorithm for calculating a Fourier transform. Rather than describing the mathematical formalism of a FFT, I will express its overall function pictorially in Figure 14.

A.9 Parseval's Theorem

Parseval's theorem illuminates the relationship between the average of the square of a function $f(t)$ and the Fourier coefficients. Assume a function $f(t)$ is represented by the following Fourier series which is periodic over the interval $[-l, l]$:

$$f(t) = \sum_{-\infty}^{\infty} c_n e^{in\pi t/l}, \quad (23)$$

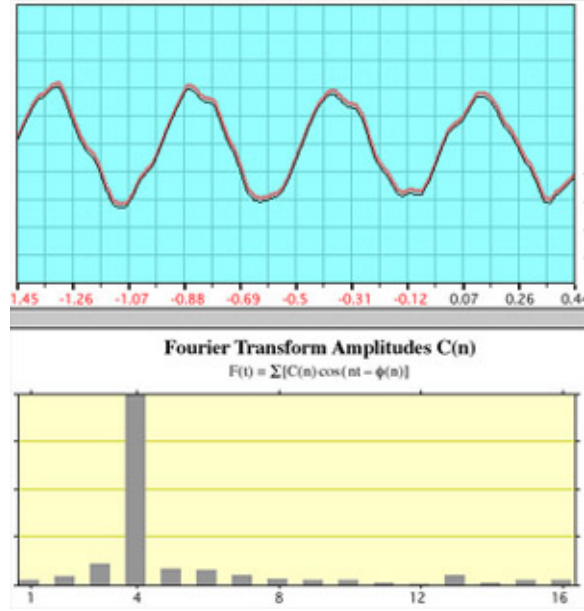


Figure 14: The bottom plot displays the FFT of the above plot. The FFT shows that most of the power is at frequency 4, reflecting the fact that four periods were chosen for the calculation of the FFT [26].

where c_n is

$$c_n = \frac{1}{2l} \int_{-l}^l f(t) e^{-in\pi t/l} dt. \quad (24)$$

Parseval's theorem then claims the following:

$$\text{The average of } |f(t)|^2 \text{ over a period} = \sum_{-\infty}^{\infty} |c_n|^2. \quad (25)$$

Parseval's theorem can be written in several different ways including the following:

$$\int_{-\infty}^{\infty} |x(t)|^2 dt = \int_{-\infty}^{\infty} |\tilde{x}(f)|^2 df, \quad (26)$$

$$\int_0^{\infty} S(f) df = \sigma^2 \quad (27)$$

where $|\tilde{x}(f)|^2$ is the energy spectral density and $S_y(f)$ is the power spectral density. Parseval's theorem can easily be related to the RMS by the inclusion of a square root.

Appendix B How to Access the Summary Pages

The 40m detector summary pages can be viewed on <https://nodus.ligo.caltech.edu:30889/detcharssummary/>, which updates every 30 minutes to represent the most recent channel outputs for the detector.

After receiving appropriate credentials, files to edit the summary pages can be found on the nodus 40m server (nodus.ligo.caltech.edu) at `/users/public_html/gwsumm-config`. All files following the pattern `c1*.ini`, in addition to `defaults.ini`, are read by a Cron job which then applies the changes found in these files to the summary page website. These files contain information on the channels that are represented and the plot format that will represent the relevant information, such as spectra, time-series, etc. There are many files for the various subsystems, such as `c1sus.ini`, `c1weather.ini`, and `c1ps1.ini`.

The processes responsible for generating the summary pages are executed from the `ldas-pcdev1` headnode at the CIT cluster using the 40m shared account. A summary page tab can be rendered manually for a specific day (`YYMMDD`) by running the command:

```
gw_summary day YYYYMMDD --ifo c1 --config-file DIRECTORY/defaults
  ↪ .ini --config-file DIRECTORY/c1sus.ini
```

from the `public_html/summary/` directory,, while linking to the `DIRECTORY` that contains all relevant `*.ini` files. This directory also contains relevant logs and error messages for recent summary pages runs.

Appendix C Laguerre Expansion

I provide a statistical background for Laguerre exponential expansions, following the method defined in [16]. We define a probability density function, $P(\zeta)$, given the following Rayleigh distribution:

$$\Phi(\zeta) = e^{-\zeta}, \quad (28)$$

where ζ is a function of Gaussian variables x and y ,

$$\zeta = \frac{1}{2}(x^2 + y^2). \quad (29)$$

We derive ζ by first defining a heterodyne signal. We focus on the signal component at $f_0 = \omega_0/2\pi$ with frequency resolution $df = 1/T$. We define this signal component as

$$v(t) = A_x \cos \omega_0 t + A_y \sin \omega_0 t, \quad (30)$$

for $f_0 \gg df$. The variables, A_x and A_y , change at a much slower rate than the frequency of oscillation, ω_0 . We can then calculate the instantaneous power of the signal to be

$$P(t) = \frac{1}{T} \int_t^{t+T} v(t')^2 dt', \quad (31)$$

which is equivalent to

$$P(t) = \frac{1}{2} (A_x(t)^2 + A_y(t)^2). \quad (32)$$

We hope to test the Gaussianity of the independent variables, A_x and A_y , with an instantaneous power of $P(t)$. If we replace A_x with x , A_y with y , and $P(t)$ with ζ , we reproduce Equation 28. Given that $P(\zeta)$ is perturbed from an exponential distribution, we represent the probability density function as a series expansion:

$$P(\zeta) = \bar{c}_0 \Phi(\zeta) + \bar{c}_1 L_1(\zeta) \Phi(\zeta) + \bar{c}_2 L_2(\zeta) \Phi(\zeta) + \dots \quad (33)$$

$L_n(\zeta)$ describes the Laguerre polynomials for ζ , following the pattern

$$L_n(\zeta) = e^\zeta \frac{d^n}{d\zeta^n} (\zeta^n e^{-\zeta}). \quad (34)$$

The first few Laguerre polynomials are explicitly described as $L_0 = 1$, $L_1 = 1 - x$, and $L_2 = \frac{1}{2}(x^2 - 4x + 2)$. Laguerre polynomials satisfy a condition for orthogonality:

$$\int_0^\infty L_m(\zeta) L_n(\zeta) \Phi(\zeta) d\zeta = \delta_{mn}. \quad (35)$$

The coefficients \bar{c}_n can be calculated with

$$\bar{c}_n = \int_0^\infty L_n(\zeta) P(\zeta) d\zeta, \quad (36)$$

resulting in coefficients such as $\bar{c}_0 = 1$, $\bar{c}_1 = 1 - \bar{\zeta}$, and $\bar{c}_2 = \frac{1}{2}(\bar{\zeta}^2 - 2)$.